Article

Synthesis of 1,6-Hexanediol from cellulose derived tetrahydrofuran dimethanol (THFDM) with Pt-WOx/TiO2 catalysts

jiayue he, Samuel P Burt, Madelyn R. Ball, Dongting Zhao, Ive Hermans, James A. Dumesic, and George W. Huber

ACS Catal., **Just Accepted Manuscript** • DOI: 10.1021/acscatal.7b03593 • Publication Date (Web): 08 Jan 2018

Synthesis of 1,6-Hexanediol from cellulose derived tetrahydrofuran-dimethanol (THFDM) with Pt-WO_x/TiO_2 catalysts

Jiayue He,[†#] Samuel P. Burt,[†,§#] Madelyn Ball,[†] Dongting Zhao,[†] Ive Hermans,[†,§]

James A. Dumesic,[†*] and George W. Huber[†*]

[†] Department of Chemical and Biological Engineering, University of Wisconsin-Madison, Madison, Wisconsin 53706, United States

[§] Department of Chemistry, University of Wisconsin-Madison, Madison, Wisconsin 53706, United States

ABSTRACT: Cellulose-derived tetrahydrofuran-dimethanol (THFDM) can be converted over Pt-WO_x/TiO_2 catalysts to 1,6-hexanediol (1,6-HDO) with up to 70% yield. This reaction involves ring-opening of THFDM to 1,2,6-hexanetriol (HTO) and then hydrogenolysis of HTO to 1,6-HDO. Hydrogen spills over from Pt sites onto WO_x/TiO_2 to reduce the W=O functional group and create Brønsted acid sites. Similar catalytic activity for THFDM conversion can be been obtained with a physical mixture of Pt/TiO_2 and WO_x/TiO_2 due to hydrogen spillover over spatially separate Pt and WO_x when a reducible support (TiO_2) is used.

Keywords: *heterogeneous catalysis, biomass upgrading, bimetallic catalyst, 1,6-hexanediol, catalyst characterization, hydrogenolysis, C-O bond cleavage, H_2 spillover*

1. Introduction

Cellulose-derived from lignocellulosic biomass is the most abundant renewable carbon resource in nature, making it a promising feedstock for the production of bio-based chemicals.[1–5] 1,6-hexanediol (1,6-HDO) is a high value chemical with a market price of \$4,400/ton,[6] an annual market size of 138,000 tons, and a global market value of approximately \$600 MM.[6] It is primarily used as a monomer for polyesters and polyurethanes.[7] The most common industrial route for 1,6-HDO production is catalytic hydrogenation of adipic acid or its esters.[7] This traditional route suffers from low yields, homogeneous chemistry involving toxic chemicals, and the non-renewable use of petroleum-based feedstocks. It would be highly desirable to develop a new route to 1,6-HDO from renewable lignocellulosic feedstocks.

Several academic and industrial researchers have studied the production of 1,6-HDO from cellulose-derived molecules. Faber reported on a three-step route for 1,6-HDO production from biomass in 1981.[8] This route involves (I) biomass depolymerization to 5-hydroxymethyl furfural (HMF) using an acid catalyst in the aqueous phase, (II) HMF hydrogenation to tetrahydrofuran-dimethanol (THFDM) with Raney®-Nickel, and (III) THFDM hydrogenolysis to 1,6-HDO over a copper chromite catalyst.[9] 1,6-HDO yields were not reported in this patent, while low HMF yields (less than 8%) from cellulose have been reported because of the formation of humins.[10–12] Similarly, Buntara *et al.* reported a method to convert HMF into 1,6-HDO, which begins with HMF hydrogenation to THFDM, followed by the ring-opening of THFDM to 1,2,6-hexanetriol (HTO), and HTO hydrogenolysis to 1,6-HDO (selectivity to 1,6-HDO was 73% at 17% conversion).[13] The authors showed a one-pot reaction of THFDM to HDO using both Rh-ReO_x/SiO_2 and Nafion SAC-13 with a 1,6-HDO yield of up to 86%. Drawbacks of this process include low catalyst activity (0.10 mol·mol Pt^{-1}· min^{-1} with THFDM conversion of 21% at 80 ^oC) and rapid catalyst deactivation due to the high solubility of the catalyst support (SiO_2) in water.[14,15] Xiao *et al.* studied 1,6-HDO production from HMF over a mixture of Pd/SiO_2 and Ir-ReO_x/SiO_2 catalysts in a H_2O/THF mixture with a 57.8% 1,6-HDO yield.[16] Chen *et al.* and our group have also demonstrated C-O cleavage of tetrahydropyran-2-methanol (THP-2M) to 1,6-HDO with Rh-ReO_x/C in the aqueous phase.[17,18] Our group has also demonstrated the same reaction from THP2M in a three-step process without the use of precious metals.[19] DuPont patented a process for 1,6-HDO synthesis by hydrogenolysis of THFDM derived from levoglucosenone (LGO) over a Pt-WO_x/TiO_2 catalyst with a reported 83% yield.[20] Little information was given about the Pt-WO_x/TiO_2 catalyst used in the

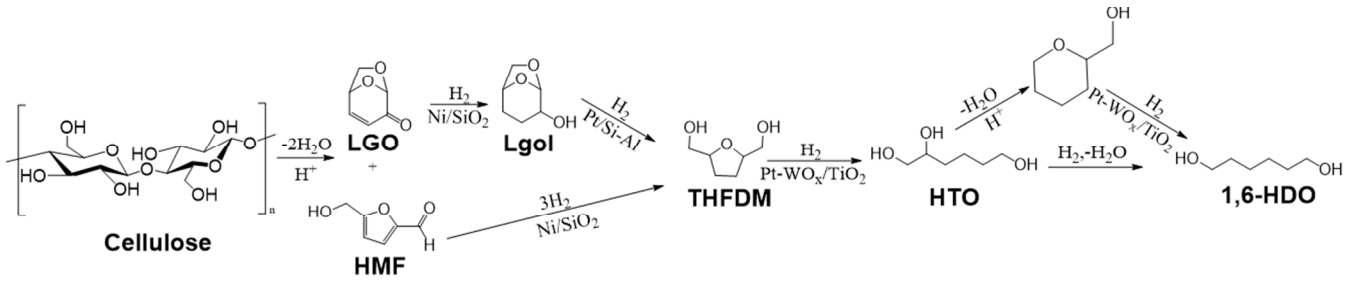

Scheme 1. Proposed reaction pathway for 1,6-HDO synthesis from cellulose.

DuPont patents, and no relationships between the structure of the catalyst and performance were given. Rennovia patented a process for the production of a mixture of HTO and 1,6-HDO from THFDM in the presence of Pt-WO_x/ZrO_2, however did not report overall yield or catalytic activity.[21] While 1,6-HDO production from biomass is currently receiving attention from both industry and academia there is a need to understand the basic chemistry and develop a relationship between the structure of the catalyst and performance. This knowledge can be used to design improved catalytic materials.

The objective of this paper is to describe the catalytic chemistry for production of 1,6-HDO from THFDM over a Pt-WO_x/TiO_2 catalyst. As we will show in this paper, the Pt-WO_x/TiO_2 catalyst has higher activity, stability and selectivity than other reported catalytic materials for this reaction. THFDM can be produced from cellulose by a route shown in **Scheme 1**. First, cellulose is extracted from lignocellulosic biomass.[22] 1,6-HDO is then synthesized from cellulose in a three step process: (I) cellulose dehydration to levoglucosenone (LGO) and 5-hydroxymethyl furfural (HMF) in the presence of dilute sulfuric acid in a tetrahydrofuran (THF)/H_2O mixture,[23] (II) LGO and HMF hydrogenation and hydrogenolysis to THFDM catalyzed by Ni/SiO_2 and Pt/SiO_2-Al_2O_3 catalysts,[24] and (III) THFDM hydrogenolysis to 1,6-HDO over a Pt-WO_x/TiO_2 catalyst.[25] As we will show in this publication, the catalytic chemistry involved in THFDM hydrogenolysis requires interaction between Pt and WO_x sites. The key objective of this paper is to elucidate the relationship between the catalyst structure and performance for THFDM hydrogenolysis over Pt-WO_x/TiO_2.

2. Experimental

Catalytic Reactions. Reactions were carried out in 50 mL HEL high-pressure batch reactors. Prior to reaction kinetics studies, the catalysts were first reduced under flowing H_2 (100 cm^3(STP)min^{-1}) (Airgas, UHP) at 250 ^oC for two hours (1 ^oC min^{-1}). The feedstock (5 wt% in H_2O) was then added to the reactor. The reactor was purged three times with H_2 prior to reaction, pressurized to the desired H_2 pressure, stirred at 700 rpm, and heated to the reaction temperature. After the reaction, the reactor was cooled in ice water and depressurized. The product mixture was then filtered using a 0.22 μm PES (polyethersulfone) syringe filter.

Products were quantified using a Shimadzu Gas Chromatograph using a Flame Ionization Detector (FID) with liquid injection. A Restek RTX-VMS capillary column (Length: 30 m, ID: 0.25 mm, film thickness: 1.4 μm) was used.

THFDM hydrogenolysis was carried out in a stainless-steel tubular flow reactor (30 cm long, 6.35 mm outer diameter), arranged in an upflow configuration and heated using a tube furnace (Thermcraft Inc. No. 114-12-1ZH). The catalyst (0.10 g) was added into the reactor with quartz wool and quartz beads packed on both sides without dilution. The catalyst was reduced under a H_2 flow (100 cm^3(STP)min−1) at 250 ^oC for 2 h before reaction. The reactor was cooled to 160 ^oC and pressurized to 500 psi H_2. An aqueous 1 wt% THFDM solution was pumped into the reactor using an Agilent Prostar HPLC pump with co-fed H_2 (40 cm^3(STP)min^{-1}). Two stainless steel tanks (150 cm^3(STP)each) were used to accumulate the liquid products at the reactor outlet. The accumulated liquid product was drained periodically into a collector container, filtered through a 0.22 μm PES syringe filter and then analyzed by GC. The gaseous products continued to flow through a back pressure regulator to maintain the reaction pressure. Both an excess flow shut-off valve and a pressure relief valve were also installed in the reactor system to ensure safe operation. The feed solutions and the liquid products were analyzed using a gas chromatograph (Shimadzu, GC-2010) equipped with a flame ionization detector (FID) and a Restek RTX-VMS capillary column. The gas effluent from the continuous flow reactor was analyzed using a gas chromatograph (Shimadzu, GC-2014) equipped with an FID and a Restek RT-Q-Bond capillary column as well as a thermal conductivity detector and a ShinCarbon ST micropacked column.

Catalyst Characterization. Raman experiments were carried out with a high-performance Renishaw InVia Raman Spectrometer equipped with a 514 nm (excitation) laser. All measurements used a 2400 l mm^{-1} grating with an efficiency of approximately 30% at 514 nm. *In situ* Raman studies used an Olympus LMPlanFL N objective with 50x magnification and a working distance of 10.6 mm. Scattered light was fil-

tered into a UV enhanced (lumogen coated) deep depleted array detector (Renishaw). The instrument was calibrated to an internal Si standard giving a Raman signal at 520.7 cm^{-1}. *In situ* measurements were taken with a fully open aperture and a 10 s exposure time, with 8 accumulations. Approximately 10 mg of sample was used for each *in situ* trial. Experiments were performed in a high-temperature cell (Linkam CCR1000) designed for temperatures up to 1000 ^{o}C. This setup uses a quartz window and water-cooled O-rings. The temperature was controlled by a Linkam T95-HT system. Gas flows during *in situ* experiments were controlled by mass flow controllers. A flow rate of 4 cm^3(STP) min^{-1} hydrogen (Airgas, UHP) was used for all reductions, and 4 cm^3(STP) min^{-1} of a 20% oxygen/helium (Airgas, UHP) mixture was used for all calcinations. Heating ramps for *in situ* reductions and calcinations were kept at 1 ^{o}C min^{-1}. Once the desired temperature was reached, it was held there for two hours. The sample was cooled to room temperature after calcination or reduction. Spectra were then taken at room temperature under 4 cm^3(STP)min^{-1} helium flow. Data were processed with the Renishaw WiRE software package.

Metal loadings of catalysts used in this study were determined by Inductively Coupled Plasma-Atomic Emission Spectroscopy (ICP-AES) after digesting the solid samples in a mixture of HCl (Sigma-Aldrich #258148), HNO_3 (Sigma-Aldrich #438073), and HF (Sigma-Aldrich #339261) at 120 ^{o}C overnight. NH_3-TPD measurements were carried out with a Micromeritics Autochem II Chemisorption Analyzer. Approximately 150 mg of sample was used for these measurements. Prior to NH_3-TPD analysis, samples were dehydrated at 400 ^{o}C for three hours (1 ^{o}C min^{-1}) under a flow of dry air (Airgas). Samples that were to be pre-reduced were then cooled to 50 ^{o}C under a flow of He (Airgas, UHP), and then heated to 250 ^{o}C for two hours (1 ^{o}C min^{-1}) under a flow of H_2 (Airgas, UHP). Samples were then cooled to 100 °C for NH_3 adsorption. Adsorption was performed for 30 min at 100 °C under a flow of 40 cm^3(STP)min^{-1} 10%NH_3–Ar (Airgas). NH_3 was desorbed under a 40 cm^3(STP)min^{-1} flow of He while heating at 10 ^{o}C min^{-1}.

N_2 physisorption measurements were performed on a Micromeritics 3flex apparatus. The samples were degassed prior to measurement for 4 h at 150 ^{o}C under vacuum. Adsorption isotherms were collected at 77 K and analyzed using the BET method.

FTIR experiments were performed with a Bruker Vertex 70 Fourier Transform Infrared Spectrometer equipped with an MCT detector. 3000 scans were averaged to give one spectrum with a resolution of 4.0 cm^{-1}. A flow-through transmission cell was loaded with approximately 50 mg of sample that was pressed into a self-supporting wafer with a diameter of 13 mm. Samples were dehydrated at 350 °C (1 °C min^{-1}, hold for 1 hour) under 10^{-7} mbar. Samples were then cooled to 25 °C, and the time-zero spectrum was taken. Pyridine was then flowed over the catalyst for 10 min by way of a bubbler with a carrier gas of dry N_2 at atmospheric pressure. The cell was then flushed with dry N_2 for 10 min to remove physisorbed pyridine. Samples were then heated at 3 ^{o}C min^{-1} to 150 ^{o}C and held for 1 hour under a flow of N_2 to further remove physisorbed pyridine. Spectra were obtained at 30 ^{o}C after cooling under flowing N_2. The Opus 7.0 software package was used to analyze the data. Each spectrum was background subtracted. The signals occurring at 1535 and 1447 cm^{-1} were integrated for Brønsted and Lewis acid sites, respectively, each corresponding to the ν_{19b} vibration for adsorbed pyridine. When needed, signals were deconvoluted using the Fityk 0.9.8 software package. Extinction coefficients of 1.3×10^6 cm^{-1} mol^{-1} and 1.5×10^6 cm^{-1} mol^{-1} were used to compare quantities of Brønsted and Lewis acid sites, respectively.[26]

Surface compositions of the carbon supports were characterized by X-ray Photoelectron Spectroscopy (XPS) using a K-alpha XPS (Thermo Scientific) instrument with a micro-focused monochromatic Al Kα X-ray source. Prior to analysis, the catalysts were reduced with flowing H_2 at 250 ^{o}C for two hours (1 ^{o}C min^{-1}), and stored in an oxygen-free environment, where they could be loaded in an air-tight sample holder for transport to the spectrometer. When it was desired to analyze oxidized samples, catalysts were treated in 1% O_2/N_2 at room temperature after reduction, and the same process was carried out. The samples were analyzed at 10^{-7} mbar pressure and room temperature. The spectra in the C1s, O1s, Pt4f, W4d, and Ti2p regions were collected over multiple scans; the number of scans was adjusted for each element (C = 15, O = 20, Pt = 60, W = 60, Ti = 20) to obtain an acceptable signal/noise ratio. The pass energy was held at 50 eV, the dwell time at 50 ms, and the energy step size at 0.2 eV for each region. Each region was integrated using the Avantage (Thermo Scientific) software package for determination of surface composition.

Scanning transmission electron microscopy (STEM) imaging was performed using a FEI Titan STEM with Cs aberration correction operated at 200 kV in high-angle

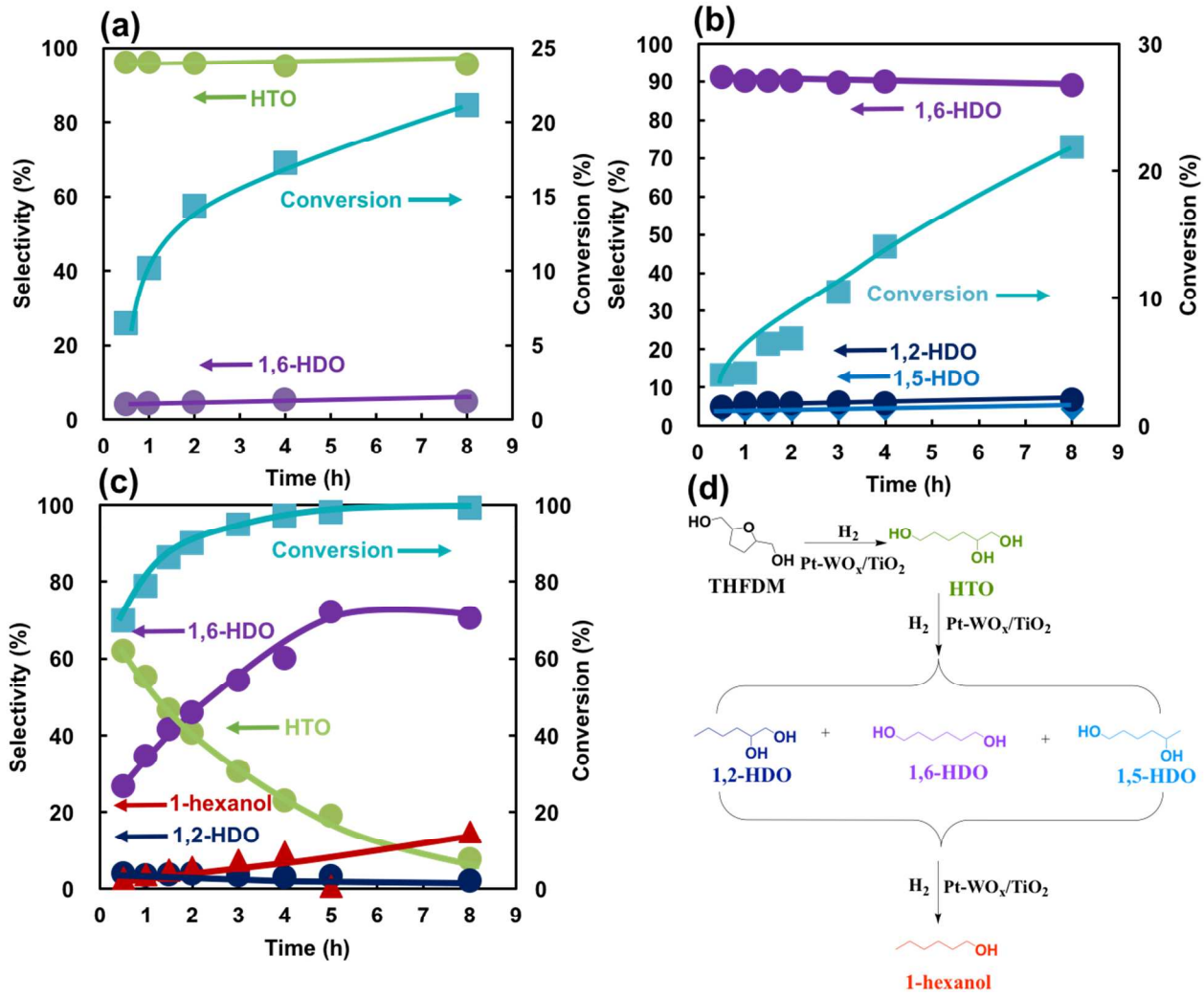

Figure 1. THFDM/HTO (5 wt% in H_2O, 20 mL) conversion over 10 wt% Pt-10 wt% WO_x/TiO_2 catalysts at 160˚C under 800 psi H_2, 700 rpm. (a) THFDM conversion in presence of 0.10 g catalysts, (b) HTO conversion into HDO in presence of 0.10 g catalysts, (c) THFDM conversion with 0.50 g catalysts. (d) proposed reaction pathway for THFDM conversion to 1,6-HDO.

annular dark field (HAADF) mode. Catalyst samples were suspended in ethanol then dropped on a holey carbon Cu TEM grid. Samples were plasma cleaned before being loaded into the microscope.

CO Chemisorption measurements were carried out with a Micromeritics Autochem II Chemisorption Analyzer. Approximately 100 mg of sample was used for each measurement. Prior to CO chemisorption, samples were reduced under 40 $cm^3(STP)min^{-1}$ 10%H_2/Ar (Airgas) to 250 ^oC (1 ^oC min^{-1}) for two hours. Samples were then cooled to 35 ^oC under 10 $cm^3(STP)min^{-1}$ He (Airgas, UHP) flow. 5%CO/He (Airgas) was then pulsed onto the catalyst in 0.5 $cm^3(STP)$ increments until consecutive signals were equal. Signals were then integrated to determine total CO consumption.

Synthesis methods of catalysts and THFDM (with 13C NMR spectrum) can be found in Supporting Information.

3. Results

Hydrogenolysis of THFDM with Pt-WO_x/TiO_2 catalysts. The conversion of THFDM over 10 wt% Pt-10 wt% WO_x/TiO_2 is shown in **Figure 1 (a)**. HTO selectivity above 95% is obtained throughout the reaction with a conversion up to 23%, while 1,6-HDO selectivity is around 5%. The HTO that is formed can be selectively (90% + selectivity) converted into 1,6-HDO, as shown in **Figure 1 (b)**. At THFDM conversions of 100% (**Figure 1** (c)), 1,6-HDO can be produced in yields above 70%. 1-hexanol and 1,2-hexanediol (1,2-HDO) are the major side products. A 1,6-HDO yield of >70% can be obtained with 10 wt.% THFDM feedstock in 8 hrs (Figure S10).

The rates of conversion of THFDM, HTO and THP-2M are shown in **Table 3**. The rate for THFDM

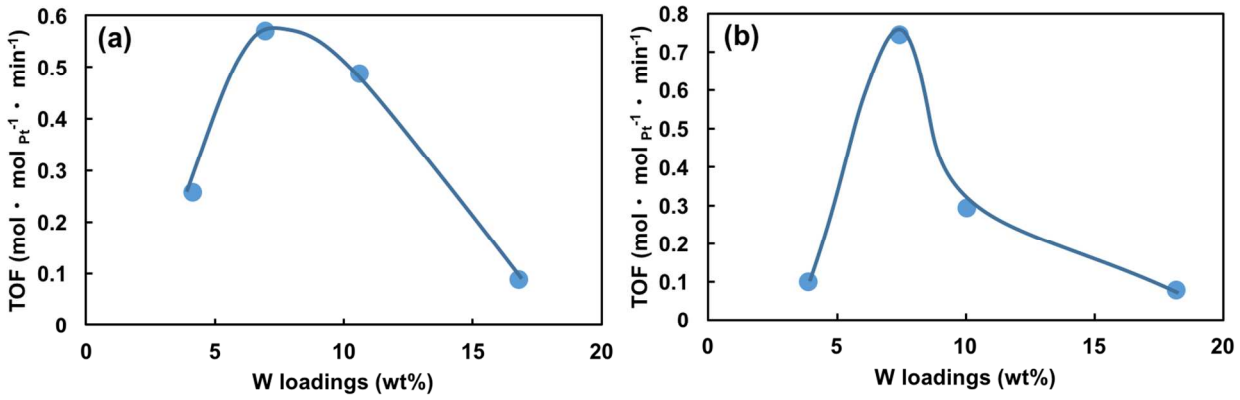

Figure 2. THFDM hydrogenolysis over Pt-WO_x/TiO_2 catalysts (a) TOFs of 4 wt% Pt-WO_x/TiO_2 as a function of tungsten loadings. (b) TOFs of 10 wt% Pt-WO_x/TiO_2 as a function of tungsten loadings.

conversion is 0.29 mol·mol $_{Pt}^{-1}$· min^{-1}. The rate for HTO conversion is 0.15 mol·mol $_{Pt}^{-1}$· min^{-1}. As reported in previous studies,[18,27] the hydrogenolysis of THFDM and THP-2M over a RhRe-based catalyst requires the presence of water to generate the Brønsted acidity of the oxophilic promoter; however, as shown in **Table 1**, the rate for THFDM conversion in THF (0.075 mol·mol $_{Pt}^{-1}$· min^{-1}) is 3-4 times lower than in H_2O (0.29 mol·mol $_{Pt}^{-1}$· min^{-1}). THP-2M undergoes hydrogenolysis in H_2O on 10 wt% Pt-10 wt% WO_x/TiO_2 at similar rates as HTO. This behavior indicates that there is a difference in the catalytic sites between Pt-WO_x/TiO_2 and RhRe-based catalysts.

Pt-WO_x/TiO_2 catalysts with various tungsten loadings and 10 wt% Pt were tested for THFDM conversion in the aqueous phase, as shown in **Figure S1**. THFDM conversion goes through a maximum at an intermediate tungsten loading. At 8 h time-on-stream the THFDM conversion increases from 5.3% with 4 wt% W loading to a maximum of 52.8% with 7 wt% W loading. The THFDM conversion then decreases to 21.5% with 10 wt% W loading and 4.5% with 20 wt% W loading. Regardless of the tungsten loadings, the combined selectivity to 1,6-HDO precursors and 1,6-HDO is ~99%.

The turnover frequency (TOF) of THFDM hydrogenolysis (on a CO chemisorption basis) as a function of tungsten loading on 4 wt% and 10 wt% Pt-WO_x/TiO_2 catalysts passes through a maximum as shown in **Figure 2(a) and (b)** and **Table S1**. The TOF for THFDM conversion over 4wt% Pt-WO_x/TiO_2 increases from 0.258 mol·mol $_{Pt}^{-1}$· min^{-1} with 4 wt% W loading to a maximum of 0.570 mol·mol $_{Pt}^{-1}$· min^{-1} with 7 wt% W loading and then gradually decreases to 0.089 mol·mol $_{Pt}^{-1}$· min^{-1} with 20 wt% W, as shown in **Figure 2 (a)**. The TOF for THFDM conversion over 10 wt% Pt-WO_x/TiO_2 increases from 0.10 mol·mol $_{Pt}^{-1}$· min^{-1} with 4 wt% W loading to a maximum of 0.75 mol·mol $_{Pt}^{-1}$· min^{-1} with 7 wt% W and then gradually decreases to 0.079 mol·mol $_{Pt}^{-1}$· min^{-1} with 20 wt% W, as shown in **Figure 2 (b)**.

Table 1 Reaction rate for conversion of THFDM, HTO and tetrahydropyran-2-methanol (THP-2M) over Pt-WO_x/TiO_2.

Reactant	**Solvent**	**Rate** (**mol·mol $_{Pt}^{-1}$· min^{-1}**)
THFDM	H_2O	0.29
THFDM	THF	0.08
HTO	H_2O	0.15
THP-2M	H_2O	0.20

The 10 wt% WO_x/TiO_2 catalyst has no catalytic activity for THFDM conversion as shown in **Table 2**. A 10 wt% Pt/TiO_2 catalyst is active for THFDM conversion, however, the rate is only 15% of the rate over 10 wt% Pt – 10 wt% WO_x/TiO_2. THFDM can be converted to HTO with a selectivity of 95% with a physical mixture of 10 wt% Pt/TiO_2 + 10 wt% WO_x/TiO_2. The rate of THFDM conversion of this physical mixture (0.25 mol·mol $_{Pt}^{-1}$· min^{-1}) is near that of the bimetallic catalyst 10 wt% Pt – 10 wt% WO_x/TiO_2 (0.29 mol·mol $_{Pt}^{-1}$· min^{-1}) and 5-6 times higher than the Pt/TiO_2 (0.044 mol·mol $_{Pt}^{-1}$· min^{-1}). Each catalyst system exhibits high selectivity to HTO (95~99%).

Table 2. Rate of THFDM conversion on Pt/Al_2O_3, Pt/TiO_2, Pt/C, WO_x/TiO_2, Amberlyst 70 and their physical mixtures. Reaction conditions: THFDM (5 wt% in H_2O, 20 mL), 800 psi H_2, 160˚C, 700 rpm.

Catalyst	**Pt cat. (g)**	**W or acid cat. (g)**	**TOF ($mol \cdot mol_{Pt}^{-1} \cdot min^{-1}$)**
5 wt% Pt/Al_2O_3	0.20	0	0.038
10 wt% Pt/TiO_2	0.10	0	0.044
5 wt% Pt/ Al_2O_3 + 10 wt% WO_x/ TiO_2	0.20	0.10	0.069
10 wt% Pt/ TiO_2 + 10 wt% WO_x/ TiO_2	0.10	0.10	0.250
5 wt% Pt/C + 10 wt% WO_x/TiO_2	0.20	0.10	0.005
10 wt% WO_x/TiO_2	0	0.10	-
10 wt% Pt-10 wt% WO_x/TiO_2	0.10	0	0.290
10 wt% Pt-10 wt% WO_x/ Al_2O_3	0.10	0	0.120
10 wt% Pt/ TiO_2 + Amberlyst 70	0.10	0.10	0.040

Approximately 5% of the W leached from the mixture of 10 wt% WO_x/TiO_2 and 10 wt% Pt/TiO_2 in an 8 hr period as determined by ICP. The W leaching is probably the reason for catalyst deactivation.

A physical mixture of Pt/TiO_2 + Amberlyst 70 has similar activity (0.042 $mol \cdot mol_{Pt}^{-1} \cdot min^{-1}$) as the Pt/ TiO_2 catalyst (0.044 $mol \cdot mol_{Pt}^{-1} \cdot min^{-1}$). Physical mixtures of Pt on non-reducible supports (Al_2O_3 or activated carbon) and WO_x/TiO_2 have much lower activity than the physical mixture of Pt/TiO_2 and WO_x/TiO_2. The HTO selectivity drops from >95% to 77-84% with the mixtures containing Pt/Al_2O_3. It is also noted that there is no conversion over the physical mixture of 5 wt% Pt/C + 10 wt% WO_x/TiO_2 after 30 mins. This behavior indicates that Pt must be on a reducible support THFDM hydrogenolysis with physical mixtures. However, the reaction rate of bimetallic 10 wt% Pt – 10 wt% WO_x/Al_2O_3 (0.12 $mol \cdot mol_{Pt}^{-1} \cdot min^{-1}$) is much higher than that of the physical mixture of Pt/TiO_2 and WO_x/Al_2O_3 (0.069 $mol \cdot mol_{Pt}^{-1} \cdot min^{-1}$) and about 40% of the rate of the THFDM hydrolysis with 10 wt% Pt – 10 wt% WO_x/TiO_2.

Pt-WO_x/TiO_2 was studied in a continuous flow reactor for 46 h as shown in **Figure S9**. The selectivity to the sum of the desired products (1,6-HDO, HTO, and THP-2M) ranged from 85 to 90%. The THFDM conversion decreases from 45% at 11 h time on stream (TOS) to 23% at 46 h TOS. The 1,6-HDO selectivity increases with time from 50 to 60%. The HTO selectivity goes from 23.6% through a maximum of 33.7%, then decreases to 27.6% with time. 1,2-HDO and 1,5-HDO are two other side products produced with selectivities from 2.4 to 3.6%.

Pt-WO_x/TiO_2 Characterization. For clarity in the proceeding sections, we would like to define two terms which will be frequently used. After the final calcination of all catalysts, they were reduced under 100 $cm^3(STP)min^{-1}$ H_2 to 250 ^oC (1 ˚C min^{-1}) for 2 hours. Catalysts were then passivated under 100 $cm^3(STP)min^{-1}$ 1% O_2/Ar for 30 minutes at room temperature, so they could be stored under ambient conditions. In some cases, catalysts were then reduced once again at 250 ˚C for 2 hours to be characterized under reducing conditions. Catalysts that have undergone this second reduction step will from now on be referred to as "reduced".

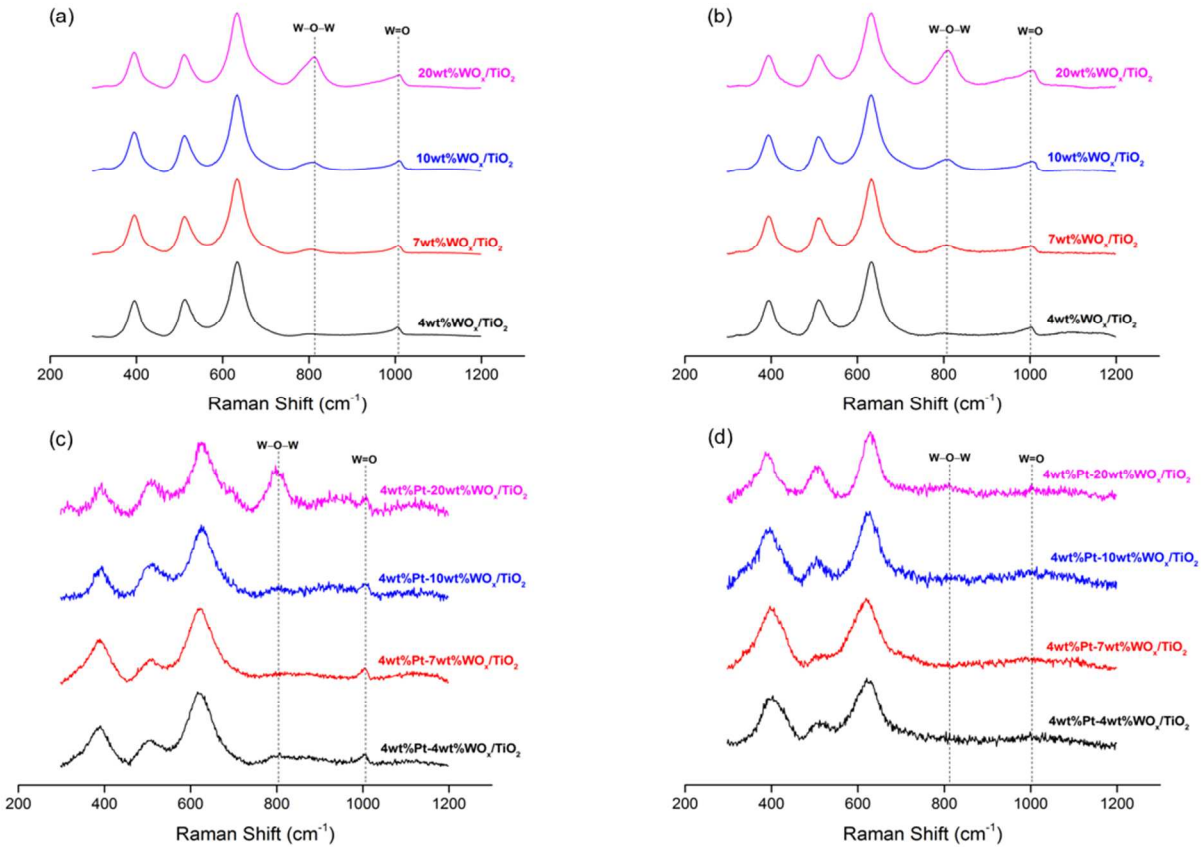

Figure 3. Raman spectra of monometallic WO_x/TiO_2 and Pt-WO_x/TiO_2 catalysts (a) WO_x/TiO_2 after 250˚C calcination under 8 cm^3(STP)/min flow of 20%O_2/N_2, (b) WO_x/TiO_2 after 250˚C reduction under 8 cm^3(STP)/min flow of H_2, (c) Pt-WO_x/TiO_2 after 250 ˚C calcination under 8 cm^3(STP)/min flow of 20%O_2/N_2, and (d) Pt-WO_x/TiO_2 after 250˚C reduction under 8 cm^3(STP)/min flow of H_2. All spectra were taken at room temperature.

Catalysts that have not undergone this second reduction step will be referred to as "passivated".

Figure 3 shows the results of Raman characterization on WO_x/TiO_2. The signals at 395, 511, and 633 cm^{-1} are representative of anatase.[28–30] The signal at 810 cm^{-1} represents W-O-W, and the signal at 1010 cm^{-1} represents W=O.[31–33] The ratio of the W-O-W signal to the W=O signal increases with increasing W loading (linear trend shown in **Figure S2**). As the WO_x particles grow, the concentration of W-O-W groups increases and the concentration of W=O groups stays relatively constant.[33]

Figs. 3 (a) and **3 (b)** show spectra of each WO_x/TiO_2 catalyst after calcination and reduction, respectively. The spectra in **Figs. 3 (a)** and **3 (b)** are essentially identical, indicating that the reduction procedure used here does not reduce WO_x/TiO_2 without Pt on the catalyst. Figs. 3(c) and (d) show the Raman spectra of the bimetallic 4 wt% Pt-WO_x/TiO_2 catalysts after calcination and reduction, respectively. The catalysts with Pt have noticeably different signals upon reduction. In **Fig. 3**, the W=O signal at 1010 cm^{-1} is visible in all catalysts, and the W-O-W signal at 810 cm^{-1} is visible in some catalysts. No WO_x signals are visible in the reduced 4 wt% Pt-WO_x/TiO_2 catalysts (**Fig 3d**). Possible causes of this disappearance in WO_x signals is the creation of W-OH sites and/or W metal, each of which are Raman inactive. Comparison of **Figs. 3 (a, b)** and **(c, d)** indicates that the W=O bond on WO_x is more readily reduced in the presence of Pt, likely by way of hydrogen spillover from a Pt particle onto the WO_x/TiO_2 surface. It was not possible to study bimetallic catalysts with Raman spectroscopy using higher Pt loadings, because there was too much light absorption to get an adequate signal to noise ratio. As a result, this and most of the proceeding characterization of bimetallic catalysts is carried out with 4 wt% Pt.

Fourier Transform Infrared (FTIR) spectroscopy of adsorbed pyridine was used to quantify the surface acidity. Pyridine was adsorbed on each catalyst after being reduced at 250 ^{o}C with flowing H_2 and dehydrated at 350 ^{o}C under vacuum to quantify the Brønsted/Lewis

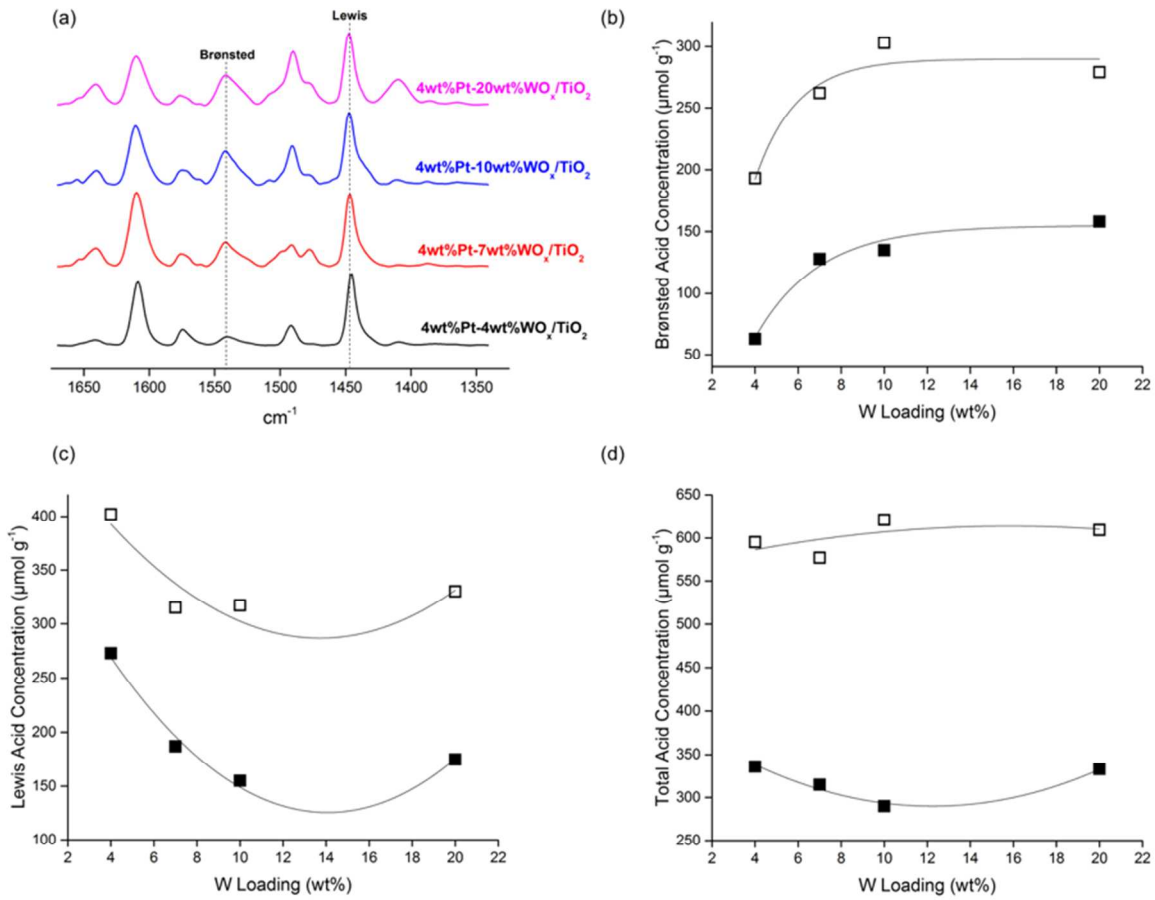

Figure 4. (a) FTIR spectra of pyridine adsorbed on 4wt% Pt-WO_x/TiO_2 catalysts after 250˚C reduction for two hours and 350˚C evacuation for 1 hour, quantification of (b) Brønsted, (c) Lewis, and (d) total acid sites at different W loadings. Open symbols represent passivated catalysts and closed symbols represent reduced catalysts.

acid ratios of each catalyst. The ν_{19b} vibration was used to quantify the relative amounts of each site. These bands appear at 1450 and 1540 cm^{-1} for Lewis and Brønsted acid sites, respectively.[34–39] Overall acid concentrations were then determined with Temperature Programmed Desorption of NH_3 (NH_3-TPD). These values are listed in **Table 3**.

Figure 4 shows the analysis of the FTIR spectra of adsorbed pyridine on 4 wt% Pt catalysts. **Fig. 4 (a)** shows the FTIR spectra of adsorbed pyridine in the 4 wt% Pt catalysts after reduction under H_2 and dehydration under vacuum. As expected and shown in **Fig. 4 (b)**, increasing W loading corresponds to increasing Brønsted acid concentration in reduced catalysts (filled squares) and passivated catalysts (open squares), presumably due to the generation of W-OH sites. Based on Raman and XPS (discussed later) data showing the reduction of WO_x in bimetallic catalysts, we believe W-OH is formed during reduction, and these FTIR data indicate that some W-OH remains after passivation. It has been proposed in previous literature[33,40,41] that Brønsted acid sites created by WO_x are important for the reactivity of PtW catalysts for similar reactions, like hydrogenolysis of glycerol, as the reactions studied here. **Fig. 4 (c)** shows that Lewis acid concentrations follow similar trends whether the catalyst is reduced or passivated. It is possible that the deposition of WO_x occupies the Lewis acid sites of the TiO_2 surface up to the WO_x monolayer. This would be shown—at low WO_x loadings—by a decrease in Lewis acid concentration with increasing WO_x loading, followed by a flattening out or slight increase of the Lewis acid concentration at the highest WO_x loadings, which is what we observe in our samples. Literature suggests that a WO_x monolayer occurs in the range of WO_x loading where our Lewis acid concentration reaches a minimum, given the TiO_2 surface area determined by N_2 physisorption (shown in the **Fig. S5**).[31] Finally, **Fig. 4 (d)** shows that the total acid concentration remains fairly constant both in reduced and passivated catalysts.

The FTIR spectra of adsorbed pyridine on 10 wt%Pt catalysts are shown in **Figure 5**. The Brønsted acid concentrations increase with increasing W loading,

with or without pre-reduction, presumably due to the creation of W-OH sites. Lewis and total acid concentrations also trendsimilar to those of the 4 wt% Pt catalysts with and without passivation. We also note that Fig. 5b shows that Brønsted acid concentrations are slightly higher in 10 wt% Pt catalysts than 4 wt% Pt catalysts at each W loading. This could be due to more generation of acidic TiO_x sites when there is more Pt on the catalyst to dissociate H_2, which can spill over onto the surface.

Table 3 shows that the total acid concentration decreases by nearly 50% in all Pt-containing catalysts, including monometallic Pt/TiO_2, during reduction. The total acid concentration for WO_x/TiO_2 does not decrease during reduction at any W loading. It appears, then, that the decrease in acid concentration during reduction is not related to WO_x species, whether on bimetallic or monometallic W-containing catalysts. **Figure 6** shows the CO chemisorption over the 10 wt% Pt and 4 wt% Pt-WO_x/TiO_2 catalysts. The quantity of adsorbed CO decreases as W is added to the catalyst. According to STEM, the 4 wt% and 10 wt%Pt particle diameters are similar at each W loading (**Figure 7 & S7**). The Pt particle size of 10 wt% Pt catalysts measured with STEM is 1.57-1.74 nm with a standard deviation of 0.58-0.78 nm. The Pt particle size of 4 wt% Pt catalysts measured with STEM is 1.13-1.45 nm with a standard deviation of 0.31-0.72 nm. The Pt particle size calculated from the CO chemisorption (assuming crystallites containing Pt are spherical and the number of surface atoms is equal to the area of the particle divided by the cross sectional area of an individual Pt site)[42] is between 2.6 and 9.8 nm for 10 wt% Pt (**Table S1**) and 3.1 and 6.6 for 4 wt% Pt (**Table 3**). These results indicate that WO_x and/or WO_x/TiO_2 migrates over a Pt nanoparticle during the catalyst pretreatment, and thereby blocks CO adsorption sites.[17,18,43] There is no decrease in CO chemisorption between monometallic 10 wt% Pt/TiO_2 and 10 wt% Pt – 4 wt% WO_x/TiO_2, indicating that the effect of WO_x blocking hydrogenation sites is minimal at such low W loadings.

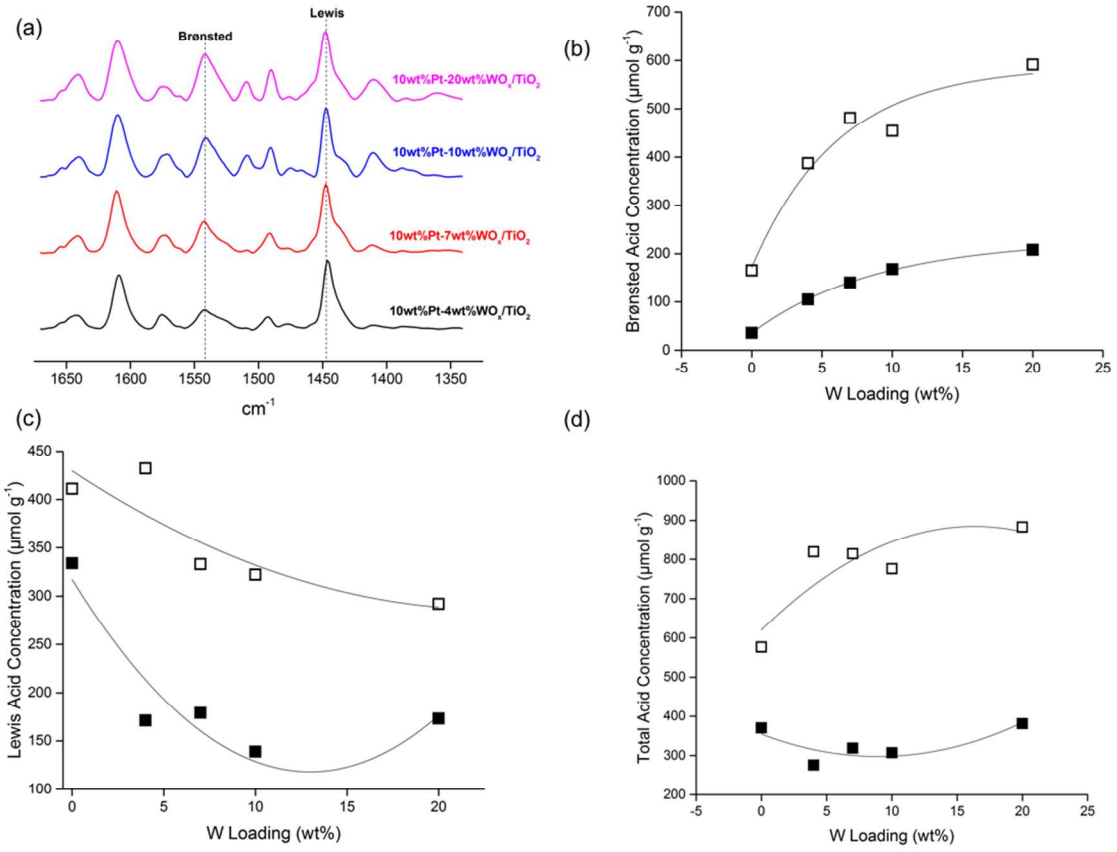

Figure 5. (a) FTIR spectra of pyridine adsorbed on 10wt% Pt-WO_x/TiO_2 catalysts after 250˚C reduction for two hours and 350˚C evacuation for 1 hour, quantification of (b) Brønsted, (c) Lewis, and (d) total acid sites at different W loadings. Open symbols represent passivated catalysts and closed symbols represent reduced catalysts.

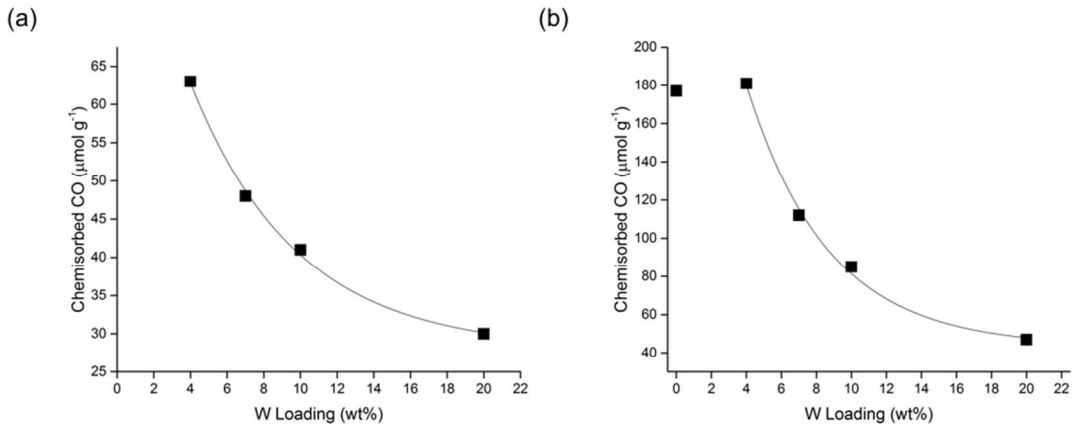

Figure 6. CO Chemisorption over (a) 4wt% Pt-WO_x/TiO_2 and (b) 10wt% Pt-WO_x/TiO_2 catalysts at different W loadings.

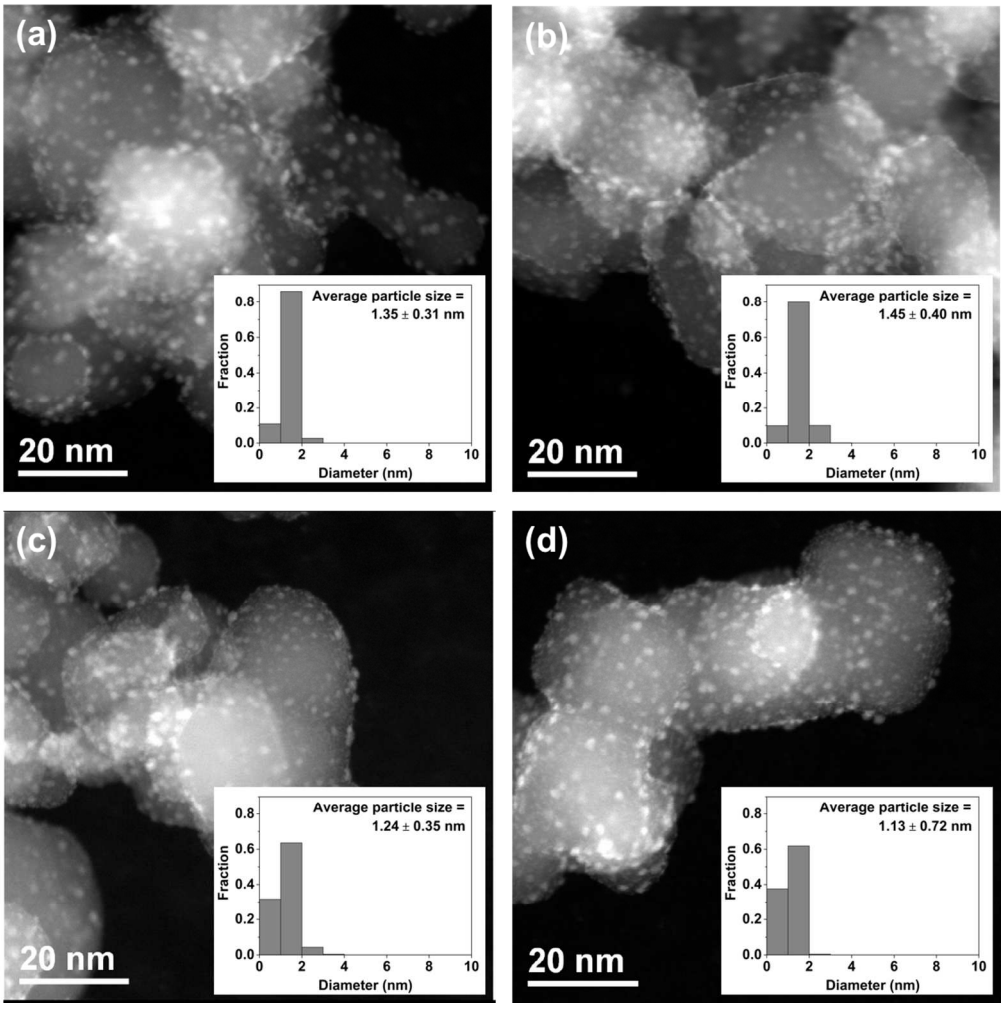

Figure 7. STEM pictures of (a) 4 wt% Pt 4 wt% WO_x/TiO_2 (b) 4 wt% Pt 7 wt% WO_x /TiO_2 **(c)** 4 wt% Pt 10 wt% WO_x /TiO_2 (d) 4 wt% Pt 20 wt% WO_x /TiO_2.

Table 3. Oxidation states, Brønsted, Lewis, and total acid concentrations, CO chemisorption and THFDM conversion rate of 4wt% Pt-WO_x/TiO_2.

Catalyst	Pt particle size (nm)		CO Uptake (μmol g^{-1})	Oxidation States (reduced catalysts)[c]		Oxidation States (passivated catalysts)[c]		Brønsted Acid Concentration (μmol g^{-1})[d]		Lewis Acid Concentration (μmol g^{-1})[d]		Total Acid Concentration (μmol g^{-1})[e]		TOF ($mol \cdot mol_{Pt}^{-1} min^{-1}$)
	STEM[a]	CO[b]		$W^{5+}:W^{6+}$	$Pt^{2+}:Pt^0$	$W^{5+}:W^{6+}$	$Pt^{2+}:Pt^0$	Reduced	Passivated	Reduced	Passivated	Reduced	Passivated	
4wt%WO_x/TiO_2	NA	NA	0	0.08	NA	0.08	NA	45	47	208	210	253	257	-
4wt%Pt-4wt%WO_x/TiO_2	1.35±0.31	3.1	63	0.23	0.04	0.04	0.36	63	193	273	402	336	595	0.258
7wt%WO_x/TiO_2	NA	NA	3	0.06	NA	0.02	NA	119	119	136	122	253	255	-
4wt%Pt-7wt%WO_x/TiO_2	1.45±0.40	4.3	48	0.25	0.07	0.09	0.69	128	262	187	315	315	577	0.570
10wt%WO_x/TiO_2	NA	NA	2	0.05	NA	0.02	NA	129	112	112	109	241	221	-
4wt%Pt-10wt%WO_x/TiO_2	1.24±0.35	5.6	41	0.14	0.13	0.09	0.19	135	303	155	317	290	621	0.488
20wt%WO_x/TiO_2	NA	NA	0	0.06	NA	0.01	NA	136	223	156	115	292	338	-
4wt%Pt-20wt%WO_x/TiO_2	1.13±0.72	6.6	30	0.07	0.12	0.05	0.40	158	279	175	330	333	609	0.089
10wt% Pt/TiO_2	1.59±0.38	3.1	177	NA	0	NA	0.30	51	110	319	466	370	576	0.044
10wt% Pt/TiO_2 + 10wt% WO_x/TiO_2 Physical Mix (1:1)	-	-	54	0.20	0.20	0.06	0.30	115	188	235	389	350	577	0.250
5wt% Pt/Al_2O_3 + 10wt% WO_x/TiO_2 Physical Mix (1:1)	-	-	25	0.13	NA[d]	0.06	NA[d]	74	53	339	202	413	255	0.069

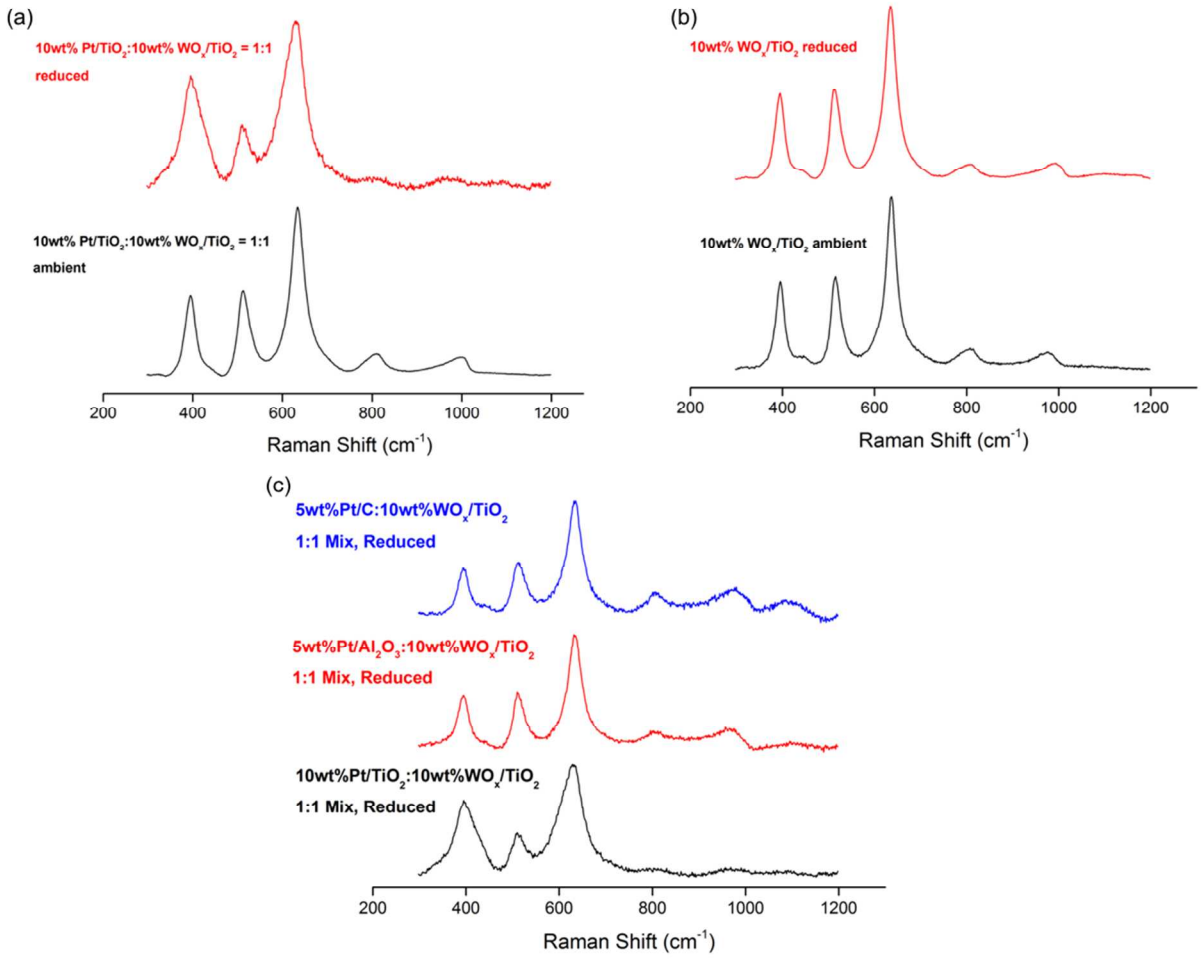

Figure 8. Raman spectra of 1:1 mixture of (a) physical mixture of 10wt%Pt/TiO_2 and WO_x/TiO_2 and (b) WO_x/TiO_2, and (c) physical mixtures of 5 wt% Pt/C, 5 wt% Pt/Al_2O_3 and 10wt%Pt/TiO_2 and WO_x/TiO_2 after reduction with 8 cm^3(STP)min^{-1} H_2 250˚C for two hours. Spectra taken at 30˚C after cooling under H_2. "Ambient" indicates these catalysts have not been reduced after passivation.

X-Ray Photoelectron Spectroscopy (XPS) was performed on each catalyst (4 wt% Pt for bimetallics) under reducing conditions to measure the W and Pt oxidation state information as shown in **Table 3**. Approximately 90% of the Pt in bimetallic catalysts is reduced to metallic sites under our reduction conditions, while some W^{6+} is reduced to W^{5+}. This will be discussed further in section 4.

Characterization of Physical Mixtures of Monometallic Catalysts. Figure 8 shows the Raman spectra of monometallic catalysts and their physical mixtures. **Fig. 8 (a)** shows the Raman spectra from the physical mixture of Pt/TiO_2 and WO_x/TiO_2 before and after our reduction treatment. The W=O and W-O-W signals disappear in this physical mixture upon reduction of the catalyst. These signals are constant during reduction of the WO_x/TiO_2 as shown in **Fig. 8 (b)**. All mixtures measured before reduction show W-O-W and W=O signals. **Fig. 8 (c)** shows that reduction of WO_x is not seen in the physical mixtures containing Pt/Al_2O_3 or Pt/C with WO_x/TiO_2. Each of these samples shows W-O-W and W=O signals before and after reduction.

The FTIR of adsorbed pyridine on the physical mixtures is summarized in **Table 3**. The mixture containing Pt/Al_2O_3 contains roughly half the acidity of 10wt% WO_x/TiO_2. The acidity of the physical mixture containing Pt/TiO_2 before and after reduction is similar to the bimetallic Pt-WO_x/TiO_2 catalyst with similar Pt and W loadings.

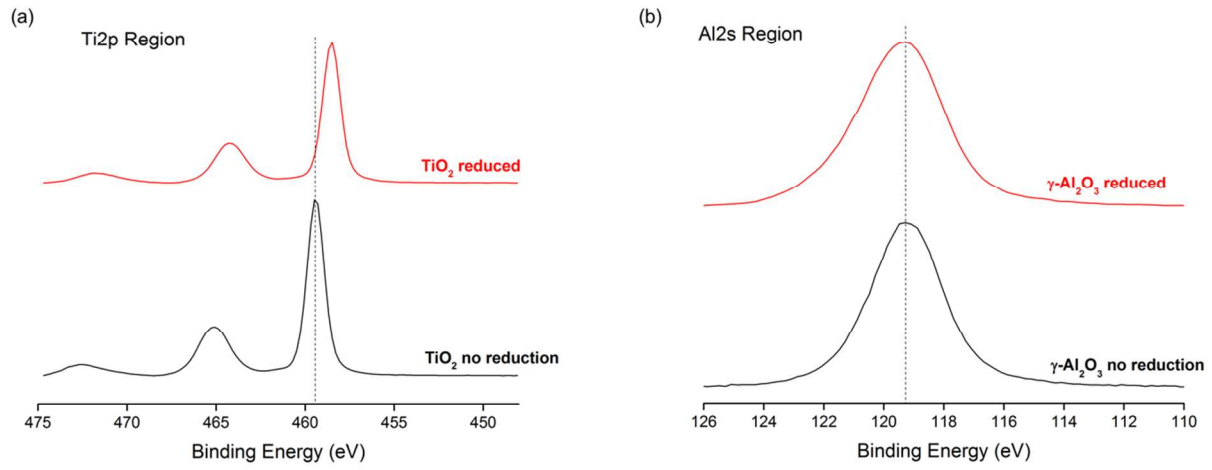

Figure 9. XPS spectra of TiO_2 (a) and γ-Al_2O_3 (b) before and after 250 ˚C treatment under 8 cm^3(STP)min^{-1} H_2 for 2 h.

The XPS results for mixtures containing Pt/TiO_2 and Pt/Al_2O_3 are shown in **Table 3**. An accurate W oxidation state for the Pt/C mixed with WO_x/TiO_2 could not be determined because the XPS spectra in this study are calibrated to the adventitious carbon signal at 284.8 eV. This signal is covered by the much larger carbon support signal in Pt/C. **Table 3** shows that the physical mixture of Pt/TiO_2 and WO_x/TiO_2 has a similar W^{5+}/W^{6+} ratio as Pt-WO_x/TiO_2 catalysts with similar Pt and W loadings. The increase in W^{5+}/W^{6+} ratio of the physical mixture containing Pt/TiO_2 during reduction is almost double that of the physical mixture containing Pt/Al_2O_3. This will be discussed further in section 4.

We examined the Ti 2p and Al 2s regions of TiO_2 and γ-Al_2O_3 to study the reducibilities of the supports themselves. **Figure 9** shows that the Ti 2p XPS signal shifts by about 1 eV to lower binding energies during reduction of TiO_2, while the reduction of γ-Al_2O_3 shows no appreciable shift in the Al 2s signal. This behavior indicates that TiO_2 is reduced under our reduction conditions, while γ-Al_2O_3 is unaffected. This supports our hypothesis that H atoms can be transferred over TiO_2, but not Al_2O_3, surfaces during reduction of physical mixtures, which is the main reason why the physical mixture containing Pt/TiO_2 can reduce WO_x and produce reactivity, while the physical mixture containing Pt/Al_2O_3 cannot. This will be discussed further in section 4. We also note that the signal positions for our TiO_2 and γ-Al_2O_3 samples without reduction treatment match literature values for TiO_2 and Al_2O_3, respectively.[44,45]

4. Discussion

The Pt-WO_x/TiO_2 catalysts presented in this publication have superior activity, selectivity, and stability for conversion of THFDM to 1,6-HDO than other catalysts reported in the literature. Buntara *et al.* [13] reported a Rh-ReO_x/SiO_2 catalyzed ring-opening of THFDM to 1,2,6-hexanetriol (HTO) with a rate of 0.013 mol·mol_{Rh}^{-1}· min^{-1}, which is 57 times slower than the 10 wt% Pt-7 wt% WO_x/TiO_2 (0.75 mol·mol_{Pt}^{-1}· min^{-1}) (**Figure 2(b)).** Both catalysts have a HTO selectivity of above 97%. Buntara et al. also showed HTO hydrogenolysis to 1,6-HDO at a selectivity of 73% at 17% conversion. As shown in **Figure 1(b)** the selectivity to 1,6-HDO with 10 wt% Pt-7 wt% WO_x/TiO_2 is 90% at 21% conversion.

Our results are consistent with the DuPont patents where they reported a process for 1,6-HDO synthesis by hydrogenolysis of THFDM derived from LGO over a Pt-WO_x/TiO_2 catalyst with a reported 83% 1,6-HDO yield.[19] Rennovia also has a patent for production of a mixture of HTO and 1,6-HDO from THFDM in the presence of Pt-W/ZrO_2 catalysts;[20] however, information about the HTO and 1,6-HDO yields and rates was not provided in the Rennovia patent.

The unique catalytic performance of Pt-WO_x/TiO_2 catalysts is due to their complex surface chemistry which includes Pt metal surface sites, W^{5+} and W^{6+} sites, and reduced TiO_2 sites. Pt particle sizes calculated by CO chemisorption are larger than the particle sizes measured directly with STEM, indicating that WO_x and TiO_x sites overcoat Pt metal sites. This behavior is similar to Rh-ReO_x/C catalysts, where the CO adsorption quantity decreased linearly with increasing Re content, whereas the metal particle sizes determined by TEM remained unchanged.[17,18,44]

The addition of WO_x to Pt/TiO_2 adds W=O sites, shown by Raman spectra of oxidized catalysts (**Figure 3**). These Raman signals disappear upon reduc-

tion of bimetallic catalysts, but remain in the case of monometallic WO_x/TiO_2 catalysts, indicating that WO_x is more readily reduced in the presence of Pt. This behavior is likely due to hydrogen spillover from Pt onto WO_x/TiO_2, which enhances the reduction of W=O signals to a species that is not Raman active. XPS supports this conclusion, showing an increase in W^{5+}/W^{6+} ratios during reduction treatment of bimetallic catalysts. Meanwhile, W^{5+}/W^{6+} ratios remain below 0.1 before and after reduction on WO_x/TiO_2. Furthermore, WO_x/TiO_2 has essentially no activity in THFDM conversion (**Table 2&3**), indicating that W^{5+} is a crucial piece of the active site for this reaction. Further supporting this hypothesis, the W^{5+}/W^{6+} ratio is maximized in 4 wt% Pt – 7 wt% WO_x/TiO_2, which is the catalyst with the maximum THFDM conversion among the 4 wt% Pt catalysts. The high THFDM conversion rate in H_2O (0.29 mol·mol $_{Pt}^{-1}$· min^{-1}), which is 3-4 times higher than THF (0.075 mol·mol $_{Pt}^{-1}$· min^{-1}) (**Table 1)**, is further evidence for hydrogen spillover on Pt-WO_x/TiO_2 contributing to THFDM conversion. As reported by Benson *et al.*, the reduction of WO_x by hydrogen spillover from Pt in Pt/WO_x is accelerated by H_2O, which can facilitate the migration of H atoms (H^+/e^- pair).[46]

A physical mixture of Pt/TiO_2 and WO_x/TiO_2 shows comparable activity as Pt-WO_x/TiO_2 when the Pt and W loadings are similar. A physical mixture of Pt/Al_2O_3 or Pt/C and WO_x/TiO_2 shows almost no reactivity. This comparison indicates that the Pt metal must be on a reducible support such as TiO_2 in order to create the active site if WO_x and Pt are not already in direct contact. This effect is shown in our Raman data of physical mixtures, where W=O signals completely disappear during reduction of physical mixtures containing Pt/TiO_2, but not in those containing Pt/Al_2O_3 or Pt/C. This indicates W=O is reduced to a Raman inactive species under our reduction conditions in physical mixtures containing Pt/TiO_2, but not in those containing Pt/Al_2O_3 or Pt/C. XPS supports this data, showing that the W^{5+}/W^{6+} ratio increases more during reduction in physical mixtures containing Pt/TiO_2 than it does in the mixture containing Pt/Al_2O_3 under the same reducing conditions. One of the roles of this support is likely to transfer H atoms across the surface from a Pt particle to a WO_x species which is not necessarily in close atomic contact. Over Al_2O_3, this process does not occur over ~15 nm from a Pt particle.[46] Over TiO_2, on the other hand, H atoms can diffuse up to micrometers from a Pt particle,[46] which explains how WO_x is able to be reduced in the physical mixture containing Pt/TiO_2.

Neither the concentration of acid sites, nor the concentration of Pt surface sites alone correlates directly with THFDM conversion over Pt-WO_x/TiO_2. Brønsted acidity increases consistently with increasing W loading in the range of 0-20 wt% W, likely indicating the generation of W-OH sites.[31,33]. Lewis and total acidity do not follow clear trends with W loading in this range. Meanwhile, CO uptake decreases consistently with W loading in bimetallic catalysts in the range of 4-20 wt% W. These results indicate migration of WO_x/TiO_2 over Pt particles during high temperature calcination/reduction, which lowers the quantity of hydrogenation sites. The maximum reactivity at intermediate W loadings shows the need for both Brønsted acid sites for C-O cleavage and exposed Pt sites for hydrogenation. This intermediate loading allows for both necessary processes to occur for reactivity. At higher W loadings, WO_x species will cover up hydrogenation sites, thereby decreasing our rates. At lower W loadings, the Brønsted acid concentration will be low, and will thereby make C-O bond scission slow and decrease our overall rates. Similarly, M. Chia *et al.* reported that the Rh-ReO_x catalyzed hydrogenolysis of THP-2M to 1,6-HDO through a bifunctional catalyst which facilitates initial acid-catalyzed carbenium ion chemistry followed by metal-catalyzed hydrogenation.[17] A likely mechanism for conversion of THFDM conversion to 1,6 HDO over Pt – WO_x/TiO_2 catalysts includes the following steps:

i. Hydrogen molecules adsorb on the Pt metal surface and dissociate to hydrogen atoms.
ii. Hydrogen atoms at the interface of Pt and TiO_2 spillover onto TiO_2. Hydrogen atoms travel in the pair of e^- and H^+. The electrons reduce Ti^{4+} to Ti^{3+} and travel through the support *via* Ti^{4+} and Ti^{3+} exchanges, while H^+ diffuse across the surface of TiO_2.[47]
iii. H atoms (H^+ and e^-) spillover/migrate to WO_x. A H atom (H^+ and e^-) reacts with a W=O species, reducing W^{6+} to W^{5+}, and creating a W-OH site, an *in situ* generated Brønsted acid site.
iv. THFDM is dehydrated by a W-OH species to form the carbenium ion. [17]
v. The carbenium ion is hydrogenated on Pt to HTO and then desorbs.

This process is then repeated for conversion of HTO into 1,6-HDO.

5. Conclusions

We demonstrate that Pt-WO_x/TiO_2 catalysts produce 1,6-HDO with a selectivity of 90% through a two-step process including (I) nearly quantitative hydrogenolysis of THFDM to HTO and (II) hydrogenolysis of HTO to 1,6-HDO. A 1,6-HDO yield up to 70% is obtained in a one-pot reaction over Pt-WO_x/TiO_2. For both 4 wt% and 10 wt% Pt-WO_x/TiO_2 catalysts, the THFDM rate goes through a maximum with W loading. Characterization data indicate that hydrogen spillover from Pt onto WO_x/TiO_2 reduces the W=O functional group on WO_x and increases the W^{5+}/W^{6+} ratio in our catalysts. The interaction between Pt and reduced WO_x plays an

important role for THFDM conversion. Nearly the same THFDM conversion is obtained from the physical mixture of Pt/TiO_2 and WO_x/TiO_2, due to the hydrogen spillover with spatially separate Pt/TiO_2 and WO_x/TiO_2. Low catalytic activity is observed with physical mixtures of WO_x/TiO_2 with Pt/C or Pt/Al_2O_3. The synergistic effect between Pt and WO_x is required for the high activity and selectivity of $Pt\text{-}WO_x/TiO_2$ and is facilitated by the reducible support.

Supplementary Information

Catalyst Synthesis techniques, as well as synthesis technique of THFDM from HMF, are listed in the Supporting Information. Tables S1-S3 and Figures S1-S10 can also be found there.

Acknowledgements

This material is based upon work supported by the Department of Energy, Office of Energy Efficiency and Renewable Energy (EERE), under Award Number DE-EE0006878. Any opinions, findings, and conclusions or recommendations expressed in this material are those of the authors and do not necessarily reflect the views of the Department of Energy. We thank Phoebe Wagner, Xiaoli Chen, Giulia Kitayama Canhetti Mondin for assistance with THFDM and catalyst synthesis and Daniel McClelland for the NMR experiments and analysis. The authors acknowledge use of instrumentation supported by UW MRSEC (DMR-1121288) and the UW NSEC (DMR-0832760).

References

(1) Werpy, T.; Petersen, G. *Top Value Added Chemicals from Biomass: Volume I- Results of Screening for potental Candidates from Sugars and Synthesis Gas*, Golden, CO, 2004.

(2) Huber, G. W.; Iborra, S.; Corma, A. *Chem. Rev.*, **2006**, *106*, 4044–4098.

(3) Centi, G.; Van Santen, R. A. *Catalysis for Renewables: From Feedstock to Energy Production*, **2007**.

(4) De bruyn, M.; Fan, J.; Budarin, V. L.; Macquarrie, D. J.; Gomez, L. D.; Simister, R.; Farmer, T. J.; Raverty, W. D.; McQueen-Mason, S. J.; Clark, J. H. *Energy Environ. Sci.*, **2016**, *9*, 2571–2574.

(5) Cao, F.; Schwartz, T. J.; McClelland, D. J.; Krishna, S. H.; Dumesic, J. A.; Huber, G. W. *Energy Environ. Sci.*, **2015**, *8*, 1808–1815.

(6) MarketsandMarkets, *1,6-Hexanediol Market by Application (Polyurethanes, Coatings, Acrylates, Adhesives, Unsaturated Polyester Resins, Plasticizers, and Others) - Trends and Forecasts to 2019*, **2014**.

(7) Werle, P.; Morawietz, M.; Lundmark, S.; Sorensen, K.; Karvinen, E.; Lehtonen, J. in *Ullmann's Encyclopedia of Industrial Chemistry*, **2008**, 263–281.

(8) Faber, M. US 4,400,468, **1983**.

(9) Buntara, T.; Noel, S.; Phua, P. H.; Melian-Cabrera, I.; De Vries, J. G.; Heeres, H. J. *Angew. Chemie - Int. Ed.*, **2011**, *50*, 7083–7087.

(10) Daorattanachai, P.; Namuengruk, N.; Viriya-Empikul, N.; Laosiripojana, N.; Faungnawakij, K. *J. Ind. Eng. Chem.*, **2012**, *18*, 1893–1901.

(11) Yin, S.; Pan, Y., Tan, Z. *Int. J. Green Energy*, **2011**, *8*, 234–247.

(12) Kuster, B. F. M. *Starch-Starke*, **1990**, *42*, 314–321.

(13) Buntara, T.; Noel, S.; Phua, P. H.; Melian-Cabrera, I.; De Vries, J. G.; Heeres, H. J. *Top. Catal.*, **2012**, *55*, 612–619.

(14) Gunnarsson, I.; Arnorsson, S. *Geochim. Cosmochim. Acta*, **2000**, *64*, 2295–2307.

(15) Siever, R. *J. Geol.*, **1962**, *70*, 127–150.

(16) Xiao, B.; Zheng, M.; Li, X.; Pang, J.; Sun, R.; Wang, H.; Pan, X.; Wang, A.-Q.; Wang, X.; Zhang, T. *Green Chem.*, **2016**, *18*, 2175–2184.

(17) Chia, M.; Pagan-Torres, J.; Hibbits, D.; Tan, Q.; Pham, H. N.; Datye, A. K.; Neurock, M.; Davis, R. J.; Dumesic, J. A. *J. Am. Chem. Soc.*, **2011**, *133*, 12675–12689.

(18) Chen, K.; Koso, S.; Kubota, T.; Nakagawa, Y.; Tomishige, K. *ChemCatChem*, **2010**, *2*, 547–555.

(19) Allgeier, A. M.; De Silva, W. I. N.; Korovessi, E.; Menning, C. A.; Ritter, J. C.; Sengupta, S. K.; Stauffer, S. US 8,865,940 B2, **2014**.

(20) Burt, S. P., Barnett, K. J., McClelland, D. J., Wolf, P., Dumesic, J. A., Huber, G. W., & Hermans, I. *Green Chem.,* **2017**, *19*, 1390-1398.

(21) Sokolovskii, V.; Lavrenko, M.; Hagemeyer, A.; Dias, E. L.; Shoemaker, J. A. W.; Murphy, V. J. US 9,586,920 B2, **2017**.

(22) Alonso, D. M.; Hakim, S.; Zhou, S.; Won, W.; Hosseinaei, O.; Tao, J.; Garcia-Negron, V.; Motagamwala, A. H.; Mellmer, M. A.; Huang, K.; Houtman, C. J.; Labbe, N.; Harper, D. P.; Maravelias, C.; Runge, T.; Dumesic. J. A. *ScienceAdvances*, **2017**, *3*(5).

(23) He, J.; Liu, M.; Huang, K.; Walker, T. W.; Maravelias, C. T.; Dumesic, J. A.; Huber, G. W. *Green Chem.*, **2017**, *19*, 3642–3653.

(24) Krishna, S. H.; McClelland, D. J.; Rashke, Q. A.; Dumesic, J. A.; Huber, G. W. *Green Chem.*, **2017**, *19*, 1278–1285.

(25) He, J.; Huang, K.; Barnett, K. J.; Krishna, S.; Alonso, D. M.; Brentzel, Z. J.; Burt, S. P.; Walker, T.; Banholzer, W. F.; Maravelias, C. T.; Hermans, I.; Dumesic, J. A.; Huber, G. W. *Faraday Discuss.*, **2017**, *202*, 247-267.

(26) Kiricsi, I.; Flego, C.; Pazzuconi, G.; Parker, W. O.; Millini, R.; Perego, C.; Bellussi, G. *J. Phys. Chem.*, **1994**, 4627-4634.

(27) Chia, M., O'Neill, B. J.; Alamillo, R.; Dietrich, P. J.; Ribeiro, F. H.; Miller, J. T.; Dumesic, J. A. *J. Catal.*, **2013**, *308*, 226–236.

(28) Deo, G.; Turek, A. M.; Wachs, I. E.; Machej, T.; Haber, J.; Das, N.; Eckert, H.; Hirt, A. M. *Appl. Catal. A Gen.*, **1992**, *91*, 27–42.

(29) Deo G.; Turek, A. M.; Wachs, I. E.; Huybrechts, R. C.; Jacobs, P. A. *Zeolites*, **1993**, *13*, 365–373.

(30) Scepanovic, M. J.; Grujic-Brojcin, M.; Dohcevic-Mitrovic, Z. D.; Popovic, Z. V. *Sci. Sinter.*, **2009**, *41*, 67–73.

(31) Wachs, I. E.; Kim, T.; Ross, E. I. *Catal. Today*, **2006**, *116*, 162–168.

(32) Ostromecki, M. M.; Burcham, L. J.; Wachs, I. E.; Ramani, N.; Ekerdt, J. G. *J. Mol. Catal. A Chem.*, **1998**, *132*, 43–57.

(33) Berton, D. G.; Shtein, M.; Wilson, R. D.; Soled, S. L.; Iglesia, E. *J. Phys. Chem. B*, **1999**, *103*, 630–640.

(34) Di Iorio, J. R.; Bates, S. A.; Verma, A. A.; Delgass, W. N.; Ribeiro, F. H.; Miller, J. T.; Gounder, R. *Top. Catal.*, **2015**, *58*, 424–434.

(35) Khaleel, A. A.; Klabunde, K. J. *Chem. - A Eur. J.*, **2002**, *8*, 3991–3998.

(36) Li, C.; Zhou, G.; Wang, L.; Dong, S.; Li, J.; Cheng, T. *Appl. Catal. A Gen.*, **2011**, *400*, 104–110.

(37) Marques, J. P.; Gener, I.; Ayrault, P.; Bordado, J. C.; Lopes, J. M.; Ramoa Ribeiro, F.; Guisnet, M. *Microporous Mesoporous Mater.*, **2003**, *60*, 251–262.

(38) Morterra, C.; Cerrato, G. *Catal. Letters*, **1991**, *10*, 357–363.

(39) Tsyganenko, A. A.; Storzheva, E. N.; Manoilova, O. V. *Catal. Today*, **2001**, *70*, 59–71.

(40) Ross-Medgaarden, E. I.; Wachs, I. E. *J. Phys. Chem. C*, **2007**, *111*, 15089–15099.

(41) Fan, Y.; Cheng, S.; Wang, H.; Tian, J.; Xie, S.; Pei, Y.; Qiao, M.; Zong, B. *Appl. Catal. B, Environ.*, **2017**, *217*, 331–341.

(42) Bartholomew, C. H.; Farrauto, R. J. *Fundametals of Industrial Catalytic Processes*, WILEY-VCH Verlag, Second Edi., **2006**.

(43) Karanjkar, P.; Burt, S. P.; Chen, X.; Barnett, K. J.; Ball, M.; Kumbhalkar, M.; Want, X.-H.; Miller, J. B.; Hermans, I.; Dumesic, J. A.; Huber, G. W. *Catal. Sci. Technol.*, **2016**, *6*, 7841–7851.

(44) Rueda, J.; Mendialdua, J.; Rodriguez, A.; Cassanova, R.; Barbaux, Y.; Gengembre, L.; Jalowiecki, L. *J. Electron Spectros. Relat. Phenomena*, **1996**, *82*, 135–143.

(45) Saha, N. C.; Tompkins, H. G. *J. Appl. Phys.*, **1992**, *72*, 3072–3079.

(46) Benson, J. E.; Kohn, H. W.; Boudart, M. *J. Catal.*, **1966**, *5*, 307–313.

(47) Karim, W.; Spreafico, C.; Kleibert, A.; Gobrecht, J.; VandeVodele, J.; Ekinci, Y.; van Bokhoven, J. A. *Nature*, **2017**, *541*, 68–71.

ASSOCIATED CONTENT

Supporting Information is attached

AUTHOR INFORMATION

Corresponding Author

*Email: gwhuber@wisc.edu
*Email: jdumesic@wisc.edu

Author Contributions

#Jiayue He and Samuel P. Burt contributed equally.

Authors are required to submit a graphic entry for the Table of Contents (TOC) that, in conjunction with the manuscript title, should give the reader a representative idea of one of the following: A key structure, reaction, equation, concept, or theorem, etc., that is discussed in the manuscript. Consult the journal's Instructions for Authors for TOC graphic specifications.